ELSEVIER

Earth and Planetary Science Letters 181 (2000) 203–216

EPSL

www.elsevier.com/locate/epsl

Analysis of Variscan dynamics; early bending of the Cantabria–Asturias Arc, northern Spain

J.M. Kollmeier, B.A. van der Pluijm, R. Van der Voo *

Department of Geological Sciences, University of Michigan, Ann Arbor, MI 48109, USA

Received 28 January 2000; accepted 6 June 2000

Abstract

Calcite twinning analysis in the Cantabria–Asturias Arc (CAA) of northern Spain provides a basis for evaluating conditions of Variscan stress and constrains the arc's structural evolution. Twinning typically occurs during earliest layer-parallel shortening, offering the ability to define early conditions of regional stress. Results from the Somiedo–Correcilla region are of two kinds: early maximum compressive stress oriented layer-parallel and at high angles to bedding strike ($D1\sigma_1$) and later twin producing compression oriented sub-parallel to strike ($D2\sigma_1$). When all D1 compressions are rotated into a uniform east–west reference orientation, a quite linear, north–south trending fold–thrust belt results showing a slight deflection of the southern zone to the south–southeast. North–south-directed $D2\sigma_1$ compression was recorded prior to bending of the belt. Calcite twinning data elucidate earliest structural conditions that could not be obtained by other means, whereas the kinematics of arc tightening during D2 is constrained by paleomagnetism. A large and perhaps protracted $D2\sigma_1$ is suggested by our results, as manifested by approximately 50% arc tightening prior to acquisition of paleomagnetic remagnetizations throughout the CAA. Early east–west compression ($D1\sigma_1$) likely resulted from the Ebro–Aquitaine massif docking to Laurussia whereas the north-directed collision of Africa ($D2\sigma_1$) produced clockwise bending in the northern zone, radial folding in the hinge, and rotation of thrusts in the southern zone.

Keywords: Hercynian orogeny; calcite; twinning; oroclines; stress

1. Introduction

The highly curved Cantabria–Asturias Arc (CAA) of northern Spain forms the core of the greater Ibero–Armorican Arc as it traces western Variscan zonations through France (Brittany) into northern Spain (Fig. 1). The Somiedo structural unit, also known as the fold nappe belt [1], marks the first occurrence of unmetamorphosed Paleozoic sedimentary units east of the basement cored Narcea Antiform [2]. Deformation continued eastward (toward the foreland) producing the Sobia unit, the Central Coal Basin (C.C.B.) [3], Ponga Unit [4], and the more easterly Picos de Europa (P.D.E.) and Pisuerga–Carrion province (P.C.P). These individual structural units vary in character commensurate with variations in lithology and changing deformation conditions. Based on deformation style and structural orientation,

* Corresponding author. Tel.: +1-734-764-8322; Fax: +1-734-763-4690; E-mail: voo@umich.edu

0012-821X/00/$ – see front matter
PII: S0012-821X(00)00203-X

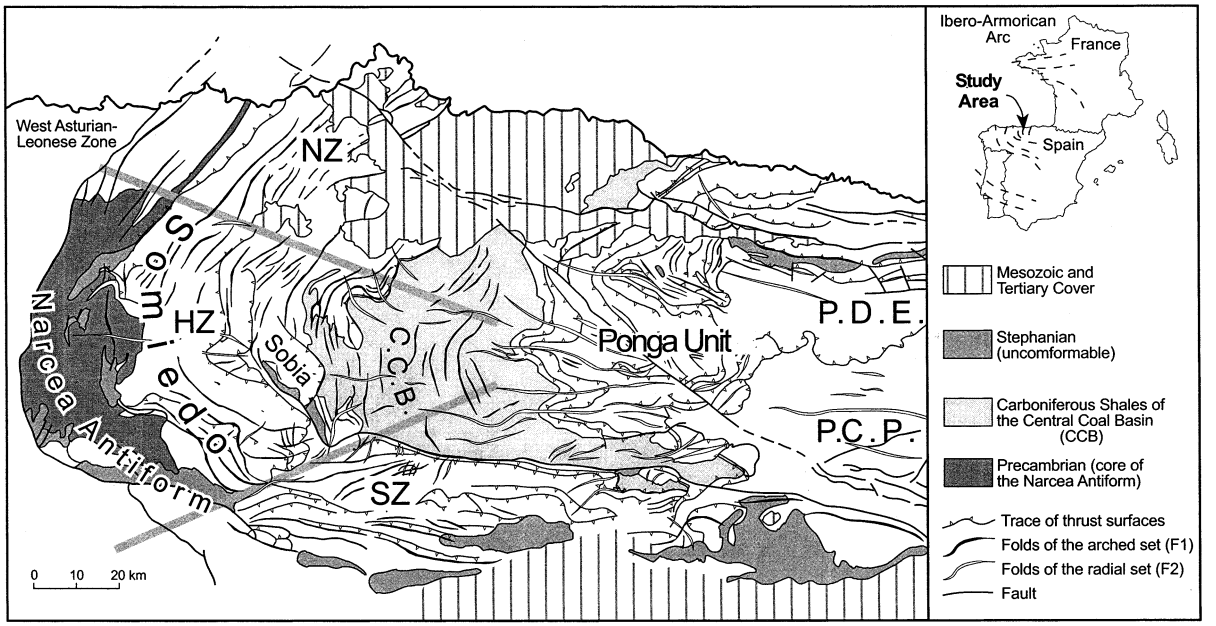

Fig. 1. Structural sketch of the Cantabrian Arc showing the traces of principal thrusts and the traces of axial fold planes that resulted from longitudinal F1 (closed) and radial F2 (open) fold sets. The Somiedo structural unit has been divided into three zones (NZ, HZ, and SZ), based on variation in structural style and orientation.

we have divided the sampled Somiedo into three zones: a northern zone (NZ), hinge zone (HZ), and southern zone (SZ).

The kinematics of arc formation, particularly arcuate foreland fold–thrust belts, has gained considerable interest since the advent of the plate tectonics [5–11]. Unraveling arc development requires contributions from as many analytical approaches as possible. However, despite extensive work in the CAA (structural, stratigraphic, paleomagnetic, seismic, and paleotemperature analyses), critical questions persist concerning the earliest conditions of foreland deformation, which correspond on a larger scale to the overall character and coeval tectonism in the convergence zone between Laurussia and Gondwana, which produced the Ibero–Armorican Arc.

Tectonostratigraphic evidence indicates that initial deformation was foreland propagating, beginning with the rear-most Somiedo structural unit in Westphalian B times and affecting the eastern-most structural units in the upper Stephanian ([12], and references therein). Spatially, a west to east geometric gradation can be seen with arcuate structural trends, averaging to a north–south trend, that gives way to ultimately east–west trending structures in the P.D.E. unit. This change in arc character has been interpreted with two end-member models: (1) an originally linear fold–thrust belt that was later bent into its present geometry (e.g. [13]), and (2) a fold–thrust belt that evolved into today's structure under a continuously changing stress field (e.g. [12]). Other interpretations have suggested an initial arc that is partially curved and later tightened [14–16] based on unfolding the radial fold set (responsible for an aerial reduction of 35–40%), displacement directions, and agreement with earlier, somewhat erroneous paleomagnetic conclusions. Paleomagnetic studies have generally concluded that (at least) half of the present curvature is secondary [17–21], rendering this an 'orocline' as defined by Carey [22]. Parés et al. [20] reevaluated published Paleozoic paleomagnetic data by applying inclination-only tilt tests and concluded that all remagnetizations are syn-tilting to post-tilting in age, thereby changing the earlier paleomagnetic conclusions to some degree. Results from Devon-

ian limestones specifically, reveal that magnetizations were recorded during and after early tilting and were affected by late vertical-axis rotations [20,23]. Thus the more recent paleomagnetic findings indicate that the horseshoe-shaped CAA resulted from late tightening of a partially curved ($\sim$50%) fold–thrust belt, leaving the amount of structural rotations prior to these remagnetizations unknown.

Calcite twinning analysis can offer an effective method for quantifying rotations in curved orogenic belts (e.g. [7,8]) complementary to paleomagnetic analysis. Previous field applications of calcite twinning analyses in fold–thrust belts include the Alps [7,8,24,25], the Idaho–Wyoming salient [26] and the Appalachians [27–30]. Experimentally deformed limestones show that individual twins record the orientation of the local state of stress as well as the orientation and magnitude of the induced intragranular strain. It is considered that stress recorded over the whole aggregate of a sample is representative of the regional stress state. Calcite twinning requires a low critical resolved shear stress ($\sim$10 MPa) [31,32] and is a strain hardening process where further twinning is resisted as beds tilt during folding [29,30,33,34]. Therefore, it typically preserves early horizontal compression prior to folding as layer-parallel shortening [27,35]. In these instances, a regional paleostress direction can be statistically determined for a sample from the array of paleostress directions of an aggregate of twinned calcite grains.

The primary objective of this paper is to determine the original geometry of the CAA that best satisfies paleostress data from deformed limestones, in addition to other constraints (paleomagnetic and regional structural data). The microstructural analysis presented here independently evaluates the kinematics of whole arc formation and provides information on the state of regional stress during Variscan deformation.

2. Geologic background and sampling

The CAA forms the eastern margin of the western Variscan orogen and is characterized by foreland-directed concavity. Two fold sets have been identified: (1) early longitudinal folds (tangential to the arc) overprinted by (2) a cross-cutting radial fold set, forming regional (Type I) interference structures [36]. Tracing the longitudinal structure of the Somiedo unit from north to south, first-order folds give way to an increasing number of thrusts (Fig. 1). The SZ is not only unique in structural style, but also shows a marked change in orientation to an overall east–west trend (with respect to the HZ; Fig. 1).

Paleozoic deposition through Carboniferous times resulted in a stable shelf sequence, generally thicker in the west (present-day coordinates) and tapering to the east. Although minor detachment zones occur in several structurally weak units throughout the lower Paleozoic sequence, the primary basal detachment soles below the Cambrian Láncara Formation [1]. Two well-exposed Devonian limestone units, the Santa Lucia and Portilla formations, were sampled to determine paleostress/strain as recorded by the mechanical twinning of calcite. These units represent conditions of a reef-rimmed carbonate platform allowing for the deposition of bioclastic grainstones and packstones with limey mudstones present [37].

Paleotemperature estimates based on conodont alteration index (CAI) values indicate maximum temperatures of 150–250°C in the Somiedo unit [38,39]. Values associated specifically to the units sampled in this paper, the Santa Lucia and Portilla formations, revealed temperatures in the range of 120–155°C and 70–95°C respectively [38]. This agrees with the observed twinning character of our samples (Fig. 2), which suggests temperatures of $\leq$200°C [40–42].

A concern in deciphering regional paleostress conditions is to avoid effects that may be associated with localized deformation. Thus, we avoided sampling near major faults, areas of high shear and fold hinges, following the recommendations of Friedman and Stearns [43]. In particular we sampled the thickest available coarse-grained beds using a portable gasoline-powered coring drill. Rock cores were oriented using a Brunton compass mounted on an aluminum core orienting device.

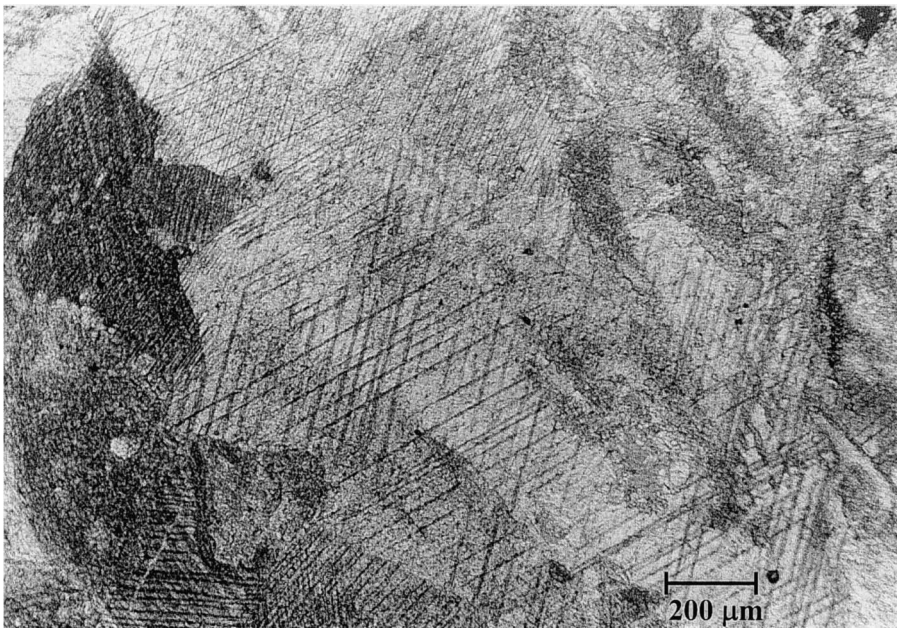

Fig. 2. A representative photomicrograph showing twinned calcite grains characterized by multiple (usually two) twin sets and thin twins indicating low temperature conditions.

3. Calcite twinning analysis

3.1. Data collection

Optical measurements define the crystallographic orientation of the twinned calcite grain (Fig. 3) as well as the twin set(s) measured. Twinning occurs most readily on *e*-twin planes in any of three orientations (twin sets) per given calcite crystal. All samples that were analyzed contained calcite grains that were not preferentially orientated crystallographically, thus ensuring that the results are not a consequence of an intrinsic fabric in the sample. Measured samples range from bioclastic grainstone to packstone containing crinoids, corals, bryozoa, and bioturbation observed in an otherwise crystalline calcite matrix. Calcite grains were observed with one, two or all three twin sets present, but most commonly contain two sets. For each grain, only twin sets that are straight and continuous within grains were measured to obtain the most accurate results. When necessary, this resulted in measurement of only one (acceptable) twin set per given calcite grain.

3.2. Analytical techniques

The use of twinned calcite as a paleostress/strain indicator in both experimentally and naturally deformed limestones has been shown to yield robust data [7,8,29,34,43–45]. Several methods are available to quantify paleostress and paleostrain with calcite twinning analysis [41,46]. To obtain compression and tension axes for each sample, we use the dynamic analysis of Turner [47]. For each twinned calcite grain, compression and tension axes (*C* and *T*, Fig. 3a) are situated 71.5 and 18.5° to the *c*-axis respectively, and at 45° to the *e*-twin plane (Fig. 3a,b). Calcite crystals have three potential *e*-twin planes (Fig. 3c), where twinning glide will occur preferentially along one plane depending on the orientation of the remote stress. Initial data were cleaned (removing all residual values (RV), see below) as suggested by Groshong et al. [48], such that populations of 25 or more twin sets remain. These are statistically significant to characterize the true twinning strain for a whole sample [48]. We have chosen the same number of twin sets as a minimum number for

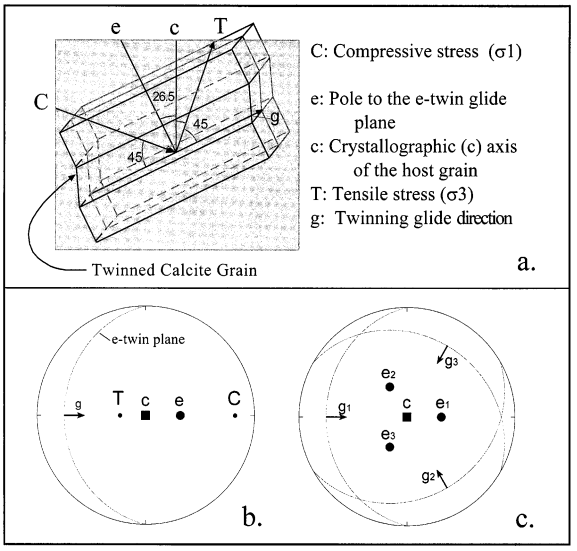

Fig. 3. (a) A calcite grain with a single *e*-twin and the compressive and tensile stress (*C* and *T*) oriented most favorably to produce twinning (oriented 45° to the *e*-twin plane). The geometric relation of *e*-twins to *c*-axis is fixed. (b) The same situation as in a but now illustrated with an equal area projection (lower hemisphere) to show the orientations of stress as related to the crystallography. (c) All three possible *e*-twin planes and their poles are represented.

computing principal stress axes as well. The resulting compression and tension axes for a sample are calculated as point means assuming a Fisherian distribution. The data are listed in Table 1.

We have applied Groshong's [49] technique to determine distributions of strain within each sample using the calcite strain gauge program of Evans and Groshong [50]. Shear strain is determined for individually measured twin sets, from which a complete strain tensor for the whole sample is statistically calculated and assigned by a least squares solution (multiple linear regression) (see [49] for a full description). If limestone is homogeneously deformed, twin sets should yield a single (positive) shear strain, which is termed the 'expected value' (equivalent to PEV in [49]). However, when a significant number of twinned grains is unfavorably oriented, the sample may have experienced multiple homogeneous or inhomogeneous strain. This results in some proportion of twin sets with opposing shear sense, referred to here as 'residual values' (RV). Thus, each grain records an expected value (EV) (shear strain) if favorably oriented, or an RV if not [49,50]. Assigning EVs and RVs depend on a twin set's orientation relative to the statistically determined direction of shear assigned for the bulk of the aggregate [49].

Experimental work of Friedman and Stearns [43] and Teufel [34] have shown that two discrete deformations may be identified using the dynamic analysis technique of Turner [47] and the strain gauge technique of Groshong [49]. Friedman and Stearns [43] concluded that superposed states of stress are distinguishable if compression axes of the dominant twin sets (EVs) are plotted separately from subordinate twin sets (RVs). Experiments by Teufel [34] indicate that larger errors are observed both in strain magnitude and orientation for samples recording two deformations. Also, a second deformation is most accurately determined when oriented at a high angle to the first; however obliquely superposed deformations can be clearly determined as well.

In presenting our data, a number of quality considerations have been included in Table 1. The first indicator of reliability is a low percentage of RV from the calcite strain gauge analysis, which reflects a largely homogeneous positive shear strain recorded by the sample. When a sample contains a high percentage of RVs, it is split into two distinct populations of twin sets (one composed entirely of EVs and the other of RVs), and each are analyzed as separate deformations. If the separation yields low percentages ($<15\%$ is used as a threshold following [34]) of newly calculated RVs, then both deformations are likely to be robust. Additionally, because the expected shear strain for the aggregate is calculated by a multiple linear regression of the data, the standard error is an additional measure of data quality [34]. Lastly, because whole-sample principal stress axes are calculated using a Fisherian statistical point mean of individual twin set stress axes, an $\alpha 95$ value is included (Table 1).

4. Results

Of the 33 sites measured from along the Somiedo unit, 26 record D1σ_1 paleostress orientations.

Table 1
Calcite twinning results for all measured samples

Sample	Raw data		Cleaned data		Strain orientations (brg.,plng.)/Elongation			Stress Orientations (brg.,plng.)			Bedding			
	N/*R* (original)	S.E.M.	*N*/*R* (treated)	S.E.M.	e_1	e_2	e_3	$\sigma 3$ (*T*)	$\sigma 1$ (*C*)	α_{95}	Strike and dip O:overturned	$S-S_0$ D1;**D2**	$\sigma 1$ ATC	$\sigma-\sigma_0$ D1;**D2**
P3E	49/1	0.372	48/0	0.388	(020,06)/2.17	(115,42)/−0.50	(284,47)/−1.67	313, 52	204, 15	9.6	180, 75w	**9**	202, −18	**26**
P3R	26/1	0.585	25/0	0.500	(268,19)/1.76	(167,30)/−0.05	(026,53)/−1.71	203, 11	316, 65	15.7	180, 75w	25	288, −03	44
P11E	27/0	3.015	27/0	3.015	(279,07)/3.26	(184,39)/0.86	(017,50)/−4.12	235, 40	23, 45	18.6	041, 73e		083, 25	
P11R	31/4	0.828	27/2	0.759	(351,56)/4.04	(228,20)/−1.57	(128,26)/−2.47	040, 13	142, 41	21.3	041, 73e		140, −31	
P13	36/5	0.572	31/0	0.324	(327,77)/2.56	(210,07)/−0.42	(118,11)/−2.14	323, 78	216, 04	18.5	219, 65w	**48**	222, 05	**46**
P16	40/1	0.804	39/0	0.707	(062,04)/2.61	(323,63)/−0.24	(155,26)/−2.37	239, 04	147, 16	9.8	063, 24s	−92	148, −08	−96
P17	40/4	2.149	36/2	2.190	(208,11)/5.83	(112,29)/−0.67	(316,58)/−5.16	066, 11	324, 46	11.9	086, 70n-O	−69	154, 18	−90
P23E	46/2	0.720	44/4	0.644	(226, 70)/3.04	(327,04)/−1.25	(058,20)/−1.78	171, 75	321, 12	12.5	134, 84s-O	**−37**	121, 05	**−55**
P23R	30/1	0.805	29/3	0.796	(269,00)/2.42	(359,01)/0.64	(151,89)/−3.07	312, 01	213, 85	15.3	134, 84s-O	−21	221, −11	−23
P453	35/0	0.602	35/0	0.602	(257,03)/2.31	(349,32)/1.19	(163,58)/−3.50	026, 22	165, 61	10.1	109, 55s	−46	183, 10	−61
S02	40/3	0.731	37/0	0.637	(120,19)/3.05	(000,55)/−0.03	(221,28)/−3.02	084, 40	241, 48	10.9	077,89n-O	−78	127, −12	−117
S07	36/1	0.614	35/0	0.627	(058,08)/3.02	(325,21)/−0.36	(169,68)/−2.65	246, 02	151, 53	12.3	076, 46s	−79	157, 08	−87
S09	37/1	1.201	36/0	1.220	(150,60)/4.05	(046,08)/−1.05	(312,29)/−3.00	111, 58	302, 32	13	187, 56w	32	300, −23	56
S10	34/4	1.390	30/0	1.054	(276,03)/1.96	(183,48)/0.76	(009,41)/−2.72	275, 01	004, 61	11	096, 85n-O	−59	183, 24	−61
S11	38/3	0.437	35/0	0.431	(056,16)/2.38	(319,22)/0.25	(179,62)/−2.64	083, 20	345, 22	15.1	102, 47n-O	−53	219, 21	−25
S12	52/10	0.450	42/0	0.311	(126,46)/1.99	(287,42)/0.38	(025,10)/−2.37	136, 62	044, 06	11.5	104, 68s		079, 57	
S20E	36/0	0.747	36/0	0.747	(314,08)/3.82	(222,18)/−0.09	(067,70)/−3.73	327, 38	137, 51	11.6	311, 72n-O		360, 17	
S20R	31/5	0.740	26/3	0.637	(058,13)/2.23	(317,41)/−0.54	(162,46)/−1.69	122, 43	317, 46	18	311, 72n-O		085, 09	
S214	57/14	0.782	43/1	0.840	(223,23)/4.77	(017,65)/−1.07	(129,09)/−3.70	225, 26	020, 63	11.4	150, 75n	−5	223, 06	−21
S221	41/3	0.796	38/1	0.770	(351,12)/3.42	(088,19)/−1.04	(242,56)/−2.38	343, 07	076, 16	11	123, 49n	−32	258, 21	14
S223E	46/0	0.624	46/0	0.624	(003,32)/2.05	(197,57)/0.67	(097,06)/−2.72	109, 58	008, 06	8.9	196, 80e	**25**	201, 09	**25**
S223R	26/0	0.966	26/0	0.966	(091,13)/3.13	(205,61)/0.62	(354,25)/−3.75	192, 04	095, 59	15.6	196, 80e	41	280, 21	36
S244	46/7	0.671	39/0	0.656	(071,31)/2.71	(338,05)/0.77	(240,59)/−3.47	092, 24	225, 58	10.8	90, 75s	−65	152, −09	−92
S277	35/6	1.271	29/1	1.044	(084,25)/4.27	(323,48)/−1.34	(190,31)/−2.94	098, 38	349, 23	13.7	098, 49n	−57	169, 23	−75
S34E	56/1	0.659	55/1	0.644	(230,37)/4.25	(352,35)/−0.87	(110,33)/−3.38	202, 52	046, 35	9.5	206, 66e	**35**	245, 01	**69**
S34R	28/2	0.890	26/2	0.776	(076,47)/4.2	(322,21)/1.03	(216,35)/−5.23	058, 28	213, 60	19.5	206, 66e	51	329, −24	85
S36E	47/3	0.920	44/0	0.868	(232,50)/3.64	(055,40)/0.77	(324,01)/−4.41	060, 53	163, 10	12.2	169, 47e-O	−2	181, 03	5
S36R	25/0	0.845	25/0	0.845	(149,01)/4.45	(058,15)/0.14	(165,73)/−4.58	178, 18	072, 44	18.7	169, 47e-O	14	264, 03	20
S43E	34/0	0.912	34/0	0.912	(336,53)/2.81	(082,11)/−0.56	(180,35)/−2.25	345, 42	207, 38	17.4	230, 74s-O	**59**	273, 07	**97**
S43R	29/1	1.216	28/0	1.184	(202,39)/2.97	(094,21)/0.67	(343,44)/−3.64	216, 18	329, 51	18.3	230, 74s-O		330, −54	
S44	35/7	0.710	28/1	0.580	(152,01)/4.13	(059,83)/0.42	(242,06)/−4.54	018, 00	107, 72	14.8	185, 87e-O	30	284, 15	40
S45	42/5	0.795	37/1	0.715	(238,31)/3.28	(357,37)/0.04	(122,37)/−3.31	242, 33	080, 56	12.2	260, 79n-O	105	315, 09	71
S48E	37/0	0.716	37/0	0.716	(026,07)/3.31	(133,65)/0.04	(293,24)/−3.34	193, 00	282, 61	12.2	223, 88w	68	297, −23	53
S48R	35/4	0.929	31/0	0.871	(286,20)/4.03	(093,70)/−0.57	(195,04)/−3.46	255, 54	051, 32	21.5	223, 88w	**52**	191,08	**15**
S49E	51/0	0.768	51/0	0.768	(185,76)/2.37	(304,07)/−0.16	(035,12)/−2.21	274, 51	025, 14	8.6	227, 48n	**56**	202, 06	**26**
S49R	28/1	1.394	27/0	1.294	(009,01)/4.43	(279,09)/−0.62	(107,81)/−3.85	038, 09	297, 55	14.1	227, 48n	72	305, 09	61
S68E	34/0	0.537	34/0	0.537	(113,39)/2.34	(311,50)/−1.01	(211,08)/−1.33	104, 32	314, 53	11.6	308, 75n		001, 09	

Table 1 (*continued*)

Sample	Raw data		Cleaned data		Strain orientations (brg.,plng.)/Elongation			Stress Orientations (brg.,plng.)			Bedding				
	N/R (original)	S.E.M.	*N/R* (treated)	S.E.M.	e_1	e_2	e_3	$\sigma 3$ (*T*)	$\sigma 1$ (*C*)	α_{95}	Strike and dip O:overturned	$S-S_0$ D1:**D2**	$\sigma 1$ ATC	$\sigma-\sigma_0$ D1:**D2**
S68R	31/4	0.783	27/0	0.716	(336, 41)/2.46	(157,48)/−0.32	(067,00)/−2.15	323, 07	101, 35	16.5	308, 75n		267, 13	
S69E	40/0	0.919	40/0	0.919	(015,32)/3.17	(142,45)/0.15	(266,29)/−3.33	042, 60	268, 22	10.2	089, 70n	**−82**	109, 08	**−67**
S69R	27/0	1.287	27/0	1.287	(233,37)/3.01	(134,11)/0.41	(030,51)/−3.42	282, 26	054, 55	15.8	089, 70n	−66	207, 02	−37
S71	30/4	1.089	26/1	0.855	(043,30)/2.76	(140,14)/0.20	(251,56)/−2.96	347, 01	256, 59	13.3	078, 64n-O	−77	202, −23	−42
S72	30/4	0.932	26/0	0.879	(072,15)/3.72	(332,31)/−0.02	(184,55)/−3.70	071, 16	295, 70	12.5	097, 73n-O	−58	206, −10	−38
S75E	49/1	0.406	48/0	0.377	(142,01)/2.54	(239,82)/1.08	(052,08)/−3.62	288, 62	044, 12	9.8	072, 74s	**−99**	067, 30	**−109**
S75R	27/2	0.939	25/1	0.819	(054,09)/4.13	(160,59)/2.41	(320,30)/−6.54	069, 18	181, 70	15.9	252, 74s	97	336, 03	92
S77E	45/1	0.588	44/0	0.545	(159,72)/2.34	(338,17)/−0.49	(248,00)/−1.86	124, 78	298, 13	9.3	140, 84s	**−31**	124, 20	**−52**
S77R	31/4	0.855	27/2	0.862	(268,07)/2.94	(360,21)/−0.34	(159,68)/−2.60	298, 20	164, 58	18.1	140, 84s	−15	202, −07	−42
S79	40/5	0.949	35/2	0.781	(280,65)/3.22	(097,25)/−0.46	(187,10)/−2.77	304, 72	137, 18	11.2	133, 89s	**−38**	151, 04	**−25**

N is the number of twin sets analyzed and *R* is the number of associated RVs. Raw data were cleaned by removing all RVs, as suggested by Groshong [48]. Both raw and treated data are presented with their respective standard errors (S.E.M.). Data are included for both the strain gauge technique of Groshong [49] in columns e_1, e_2 and e_3 as well as the dynamic analysis of Turner [47] in columns $\sigma 3$ (Tension), $\sigma 1$ (Compression), and α_{95}. Strike and dip and compression direction (σ_1) after tilt correction (ATC) are given with the proper deviations ($S-S_0$, $\sigma-\sigma_0$) plotted in Fig. 8a,b (D2σ_1 deviations used in Fig. 8b are in boldface).

Of these 26 samples, 13 record a second twin-producing deformation D2σ_1 (Table 1; Fig. 4). Two additional samples (P13A, S79A) record only directions that agree best with D2σ_1 based on the orientation of the recorded stress relative to structural trend. The remaining five samples are not interpretable for one of two reasons. (1) Compressions are oriented at steep angles to bedding ($\geqslant 25°$), indicating twins that probably reflect local perturbations or are syn- to post-folding (e.g. sites S12, S43R, Fig. 4). (2) Multiple deformations may be present but are not distinguishable in a sample, perhaps due to local rotation and tilting of folds during arc tightening (in that case compressions are intermediately oriented between strike normal and strike parallel, e.g. sites P11, S20, S68, Fig. 4).

Samples recording two deformations typically indicate D1σ_1 and D2σ_1 to be oriented at high angles to each other. It has previously been established that longitudinal structures (tangential to the arc) belong to an early deformation that has been overprinted by a later, radial fold-producing event [1]. This forms the basis by which we interpret D1σ_1 and D2σ_1 in samples recording two twinning events. Maximum compressive stress is considered D1σ_1 when oriented (nearly) layer-parallel and at a high angle to strike of folded beds (does not fall under uninterpretable category 1 above). This occurrence illustrates the characteristic behavior of twinned calcite to record layer parallel paleostresses and strains that are passively rotated with subsequent folding within the same overall stress field (compression directed at a high angle to the hinge line). This allows for distinction of D1σ_1 compression oriented at a high angle to strike and D2σ_1 sub-parallel to strike (does not fall under uninterpretable category 2 above). One exception, sample S43, illustrates that D1σ_1 (S43R) is uninterpretable (category 1, above) whereas D2σ_1 (S43E) is robust (Fig. 4)

Whether a sample records one or two deformation events appears to be related to its location in the region (Fig. 5). Samples that record two events are nearly ubiquitous in the HZ whereas a single deformation dominates samples of the SZ. In the NZ, five of seven samples record D1σ_1 directions and four preserve D2σ_1 compres-

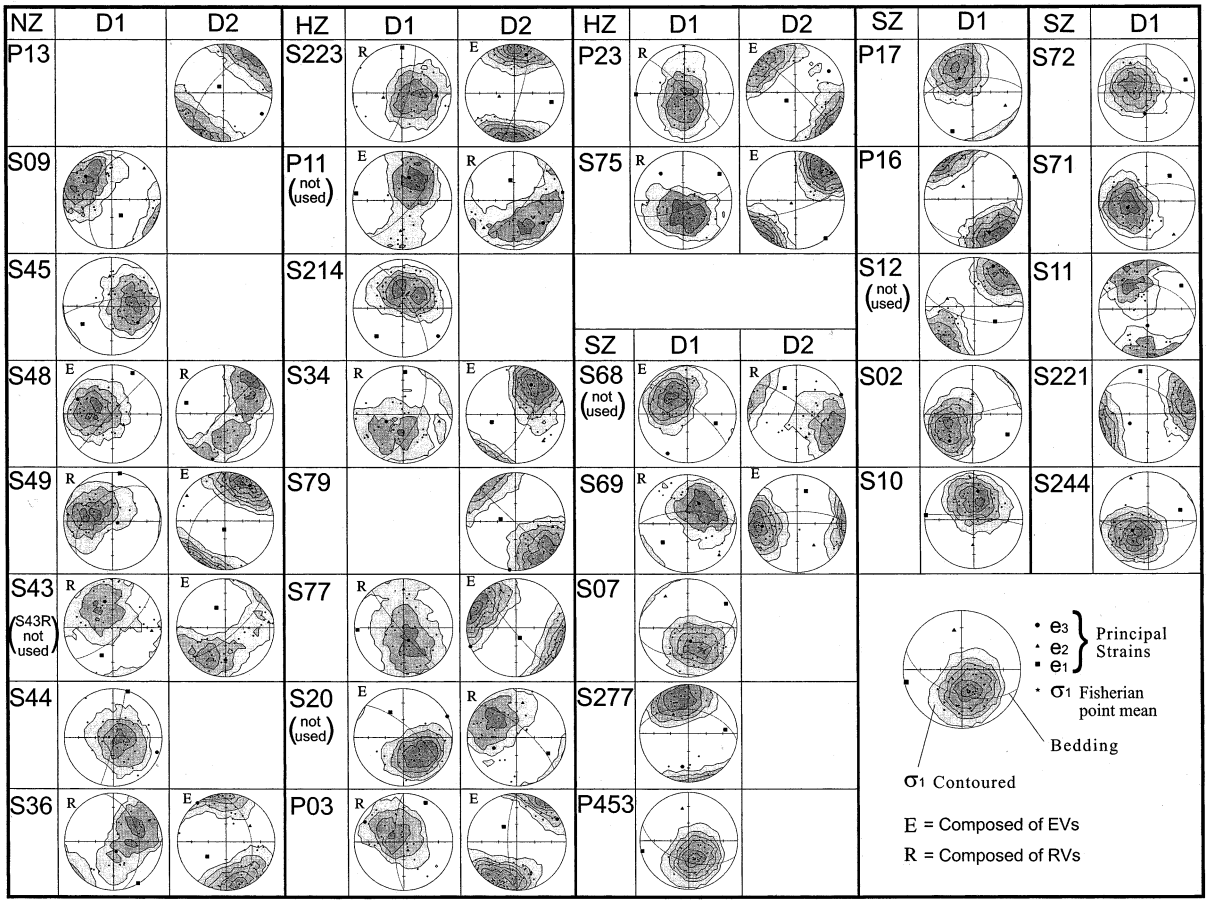

Fig. 4. Equal-area lower-hemisphere plots of all sample results. Contoured compressive stress axes are shown as well as the principal strain axes calculated with the strain gauge of Groshong [49]. All data are represented in present-day field coordinates with bedding included. Tabulated D1σ_1 and D2σ_1 compressions illustrate the predominance of D2 associated with EVs and D1 associated with RVs. Stress data are contoured with the fixed-circle counting method of Kamb, whereas maximum compressive stress directions are calculated as point means assuming a Fisherian distribution.

sion as determined by the relationship between stress orientations and strike. The results are shown in map view in Fig. 5.

5. Discussion

5.1. D1 folding and thrusting

All three structural zones of the Somiedo unit are unbent to an earliest geometry by rearranging D1 stresses to an arbitrarily uniform (present-day) east–west reference orientation. What results is an essentially linear, generally north–south trending fold–thrust belt (Fig. 6). However, the SZ features a mild foreland-progressive counter-clockwise rotation in successively younger thrust sheets, which culminates in a more southeasterly trend in the frontal portion. This structural deflection results perhaps from a greater foreland translation via thrusting relative to the HZ and NZ. Averaging the resultant structural trends from the youngest sampled thrust sheets, we derive an orientation of 27° east of south as a best-fit D1 structural trend for all SZ samples.

Furthermore, the reconstruction in Fig. 6 is il-

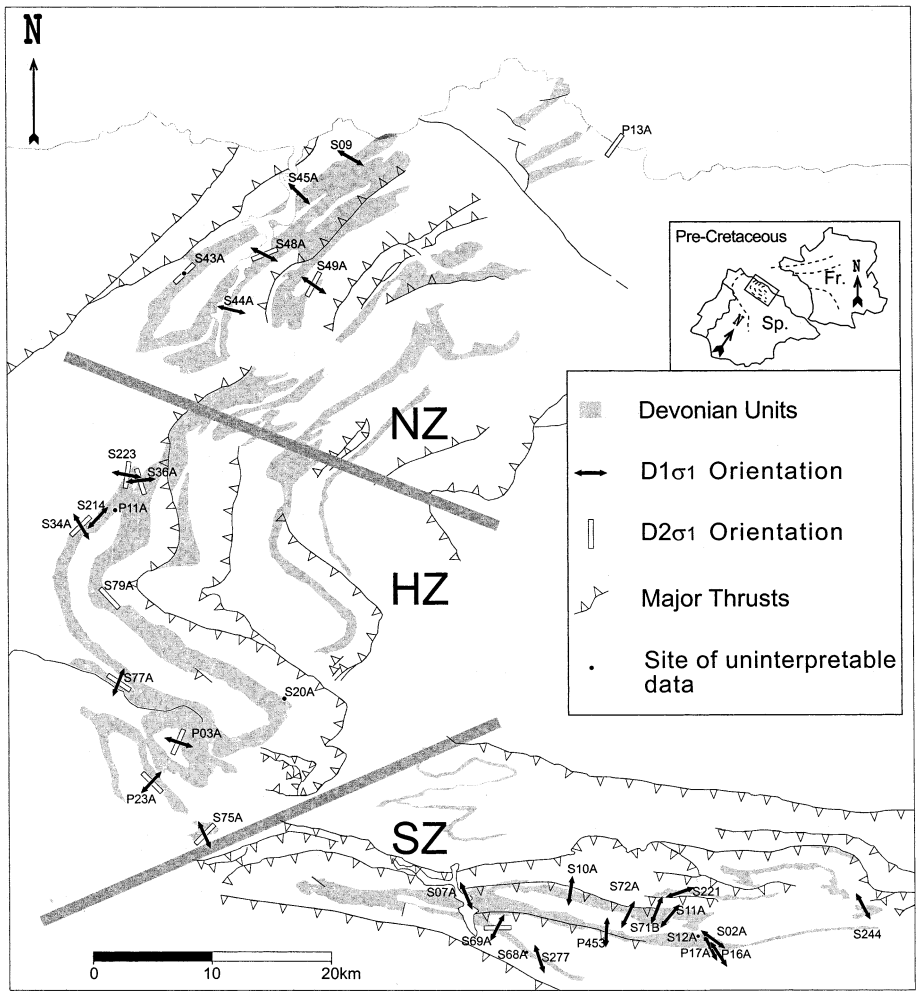

Fig. 5. Map of the CAA adapted from 1:200 000 scale geological maps [53]. Black arrows indicate the orientation of (tilt-corrected) subhorizontal $D1\sigma_1$ and white bars represent later (in situ) $D2\sigma_1$; because $D2\sigma_1$ is generally strike parallel, in situ and tilt-corrected orientations are approximately the same. The three structural zones are delineated and labeled as NZ, HZ, and SZ. See Fig. 4 for a more detailed stress to strike relation as local structures may deviate from the generalized trends (e.g. S214).

lustrated by a series of three equal-area lower-hemisphere projections of D1 maximum compressive stress axes (Fig. 7). Stress directions in present-day structures (Fig. 7a) are first untilted to paleohorizontal (Fig. 7b), and then rotated about a vertical-axis to the original geometry presented in Fig. 6 (Fig. 7c). Even with the scatter due to assigning all SZ sites an average D1 trend of S 27 E (open symbols, Fig. 7c), the resulting alignment illustrates that uniform as well as nearly bedding-parallel compressions are valid assumptions. In a very generalized fashion, Fig. 7 illustrates an overall fold and strike test for the entire study area.

5.2. Arc rotations

When considering whether a curved orogenic belt is either a primary feature (no rotation), or an 'orocline' as put forth by Carey [22], plotting structural trend versus pre-bending paleomagnetic declination poses a powerful evaluation of rota-

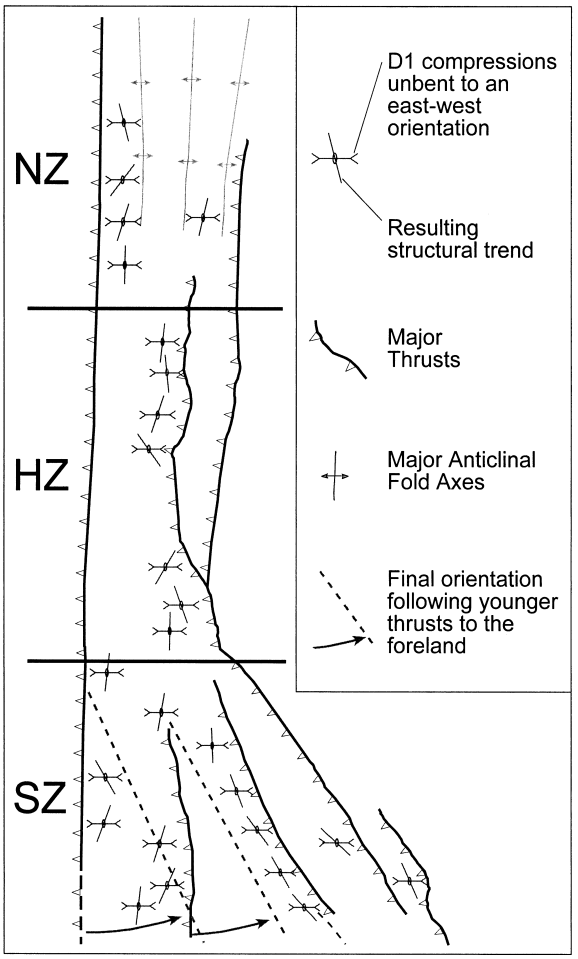

Fig. 6. Arc geometry during D1σ_1 constrained by untightening the arc to a reference east–west stress field. North–south trending thrusts in the SZ have swept eastward in a foreland progressive sequence as shown by arrows. Thin, short horizontal lines (doubly tipped with inward arrows) represent compressive stress and are related with the structural trend (thicker intersecting lines) for all 26 D1 compressions.

tion [9,20,51]. We use an analogous relationship in Fig. 8, where the axes represent the deviation from a reference strike (abscissa) and deviation from a reference D1 maximum compressive stress (ordinate). This plot can then be interpreted in terms of relative rotations, with the assumption that all stress was uniform within a single event. The likelihood of this assumption is later evaluated by comparing the plots of both deformation episodes (D1 and D2). Reference values (S_0 and

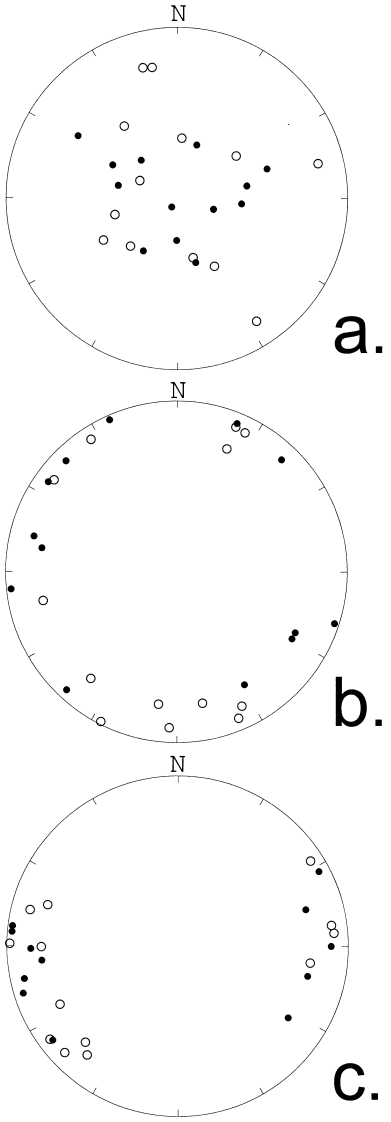

Fig. 7. Equal area lower hemisphere projections representing D1σ_1 orientations of all samples considered to unbend the CAA. Samples from the NZ and HZ are indicated with solid circles and SZ samples are denoted with open circles. Orientations from in situ data (a) are untilted to paleohorizontal (b). Finally, the data are rotated to a reference north trending structure for NZ and HZ samples, and an average structural trend of S27E for all SZ samples (c). The scatter in the SZ data illustrates the variation in stress directions in successive thrust sheets that is comparable to the NZ and HZ scatter combined.

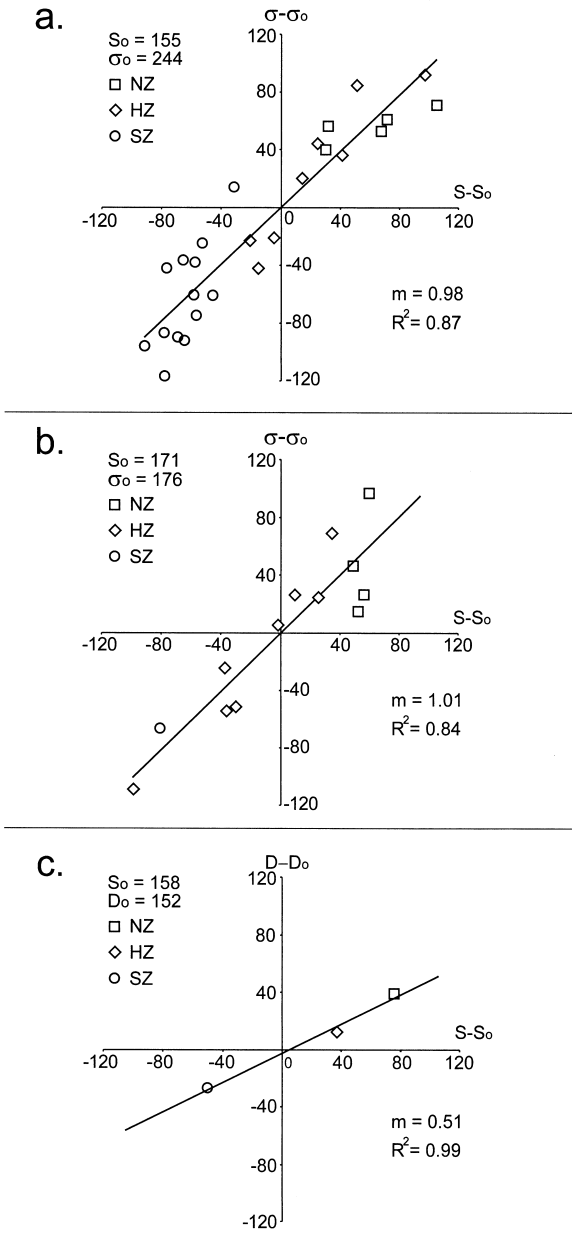

Fig. 8. (a) D1 compression deviations from the mean reference stress ($\sigma_0 = 244°$) of all 26 samples tilt corrected to bedding horizontal plotted against strike deviations from the reference strike ($S_0 = 155°$). (b) Likewise, D2 compression deviations from the mean reference stress ($\sigma_0 = 176°$) of 13 samples plotted against strike deviations from a reference strike ($S_0 = 171°$). In both cases, a linear regression is drawn with associated correlation coefficients R^2 and slope m (indicating the CAA was oroclinally bent from a nearly straight original configuration, $m = \sim 1$). (c) Paleomagnetic data [20] for the CAA showing deviations in (mean) declination and strike for each of the three zones (NZ, HZ, and SZ), illustrating rotation for approximately half of the CAA curvature.
←

σ_0 in Fig. 8a,b) are chosen merely to produce a best-fit line that passes through the origin when considering all samples. Plotted points represent the deviation from these reference values ($S_0 - S$, $\sigma_0 - \sigma$), and data are presented with maximum compressive stress axes untilted to paleohorizontal (Table 1). Fig. 8a plots D1 paleostress orientations of individual sample sites from around the arc. Ideally, if a curved orogen is a primary feature and a uniform stress field produced the original curvature, one would expect uniform stress orientations irrespective of the structural trend. This end-member condition would produce a line along the abscissa with zero slope (no deviation in σ1 orientations). The other end-member is an initially linear belt, where during bending the recorded stress directions are rotated passively with the curved geometry; in this case the expected slope of the best-fit line is 1. Fig. 8a shows that the results for the CAA correspond nearly perfectly to the latter end-member model; i.e., curvature from an originally straight belt. Note that this plot does not assess whether an originally linear structure undergoes continuous or episodic rotation, but merely indicates total rotation.

5.3. D2 folding and thrusting

In Fig. 8b the deviation from a reference D2 maximum compressive stress is plotted. A slope of ~ 1 is again observed which indicates that D1 arc geometry was nearly linear and that D2 was recorded prior to arc bending. The agreement between the rotations required for both D1 (Fig. 8a) and D2 (Fig. 8b) provides conclusive evidence of tightening with nearly all of the curvature being secondary and supports the assumption of uniform compression for each event.

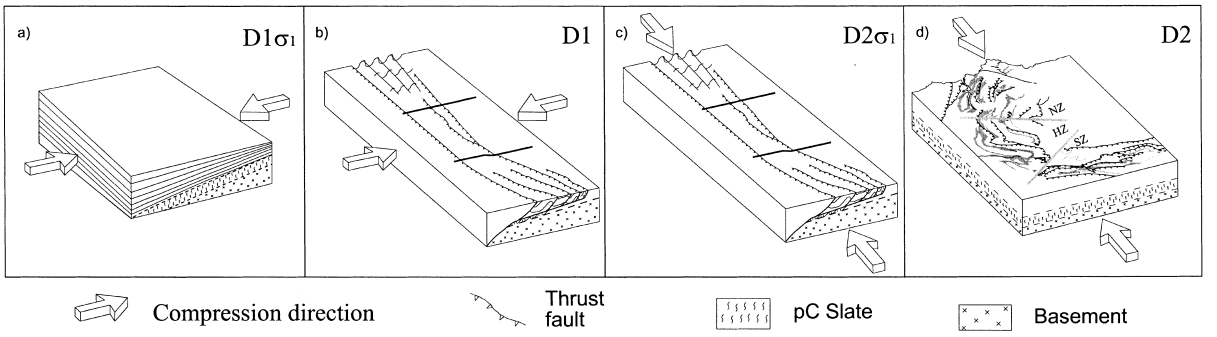

Fig. 9. Block diagrams summarizing the evolution of arc tightening beginning with east–west horizontal compression acting on a stable margin in (a) and resulting in an arc geometry (b) after D1 folding and thrusting (as in Fig. 6). A later north–south horizontal compression (D2) is shown in (c) and leads to clockwise bending in the NZ, radial folding in the HZ, and tightening of thrusts in the SZ of present-day arc geometry (d).

5.4. Evolution of the CAA

In samples recording two deformations, particularly those of the NZ and HZ, $D2\sigma_1$ is commonly oriented sub-perpendicular to $D1\sigma_1$ (Figs. 4 and 5). In the D1 fold geometry this results in $D2\sigma_1$ compressive stresses averaging to an essentially north–south orientation. Thus, analogous to D1 (Fig. 8a), $D2\sigma_1$ twinning occurs prior to the later (D2) phase of macroscopic deformation of the belt (Fig. 8b). Overall, this suggests that D2 produced clockwise bending in the NZ, radial folding in the HZ, and tightening of thrusts in the SZ. It is also observed that the SZ shows the least amount of evidence of D2 as the samples record only D1 maximum compressive stress directions in all but two samples.

Fig. 8c is a compilation of paleomagnetic data for the CAA plotting the averages for each structural zone [20]. The calculated slope is ~ 0.5, indicating that the overall arc curvature was about 50% at the time the pervasive syn-tectonic remagnetization was acquired. In comparison with the paleomagnetic results, the calcite twinning data therefore demonstrate that $\sim 50\%$ of the curvature was attained prior to the remagnetization, but following D2 calcite twinning.

Fig. 9 presents our interpretation of the evolution of the CAA in sequential block diagrams, beginning with flat lying shelf units recording pre-folding twinning due to a uniform (present-day) east–west compression ($D1\sigma_1$; Fig. 9a). During D1, longitudinal structural trends form in a nearly linear belt (Fig. 9b). $D2\sigma_1$ reflects a change in stress field from east–west to north–south acting upon the previously formed D1 structures (Fig. 9c). Lastly, present-day structural geometry reflects large scale folding (D2, manifested in radial folds and regional curvature) in response to north–south compression (Fig. 9d). A tectonic explanation for these events would be an east–west collision between the Ebro–Aquitaine massif and the Laurussian margin (D1), followed by a greater, perhaps protracted north-directed collision of Gondwana with Laurussia [52].

Acknowledgements

We thank J.C. Larrasoaña and J. Parés for their assistance in the field and J.H. Harris for his advice in calcite twinning analysis. We also thank M.A. Evans and R.H. Groshong for use of the CSG-22 program. Thoughtful reviews by D.A. Ferrill, B. Ward, and M. Burkhard improved the manuscript and are greatly appreciated. Support for this project was from National Science Foundation Grant EAR 9705755. In addition, funding for the fieldwork came from a Geological Society of America research grant awarded to J.M. Kollmeier as well as the Scott Turner fund, Dept. of Geological Sciences, the University of Michigan.*[AC]*

References

[1] M. Julivert, Decollement tectonics in the Hercynian Cordillera of northwest Spain, Am. J. Sci. 270 (1971) 1–29.

[2] G. Gutiérrez-Alonso, Strain partitioning in the footwall of the Somiedo Nappe: Structural Evolution of the Narcea tectonic window, NW Spain, J. Struct. Geol. 18 (1996) 1217–1229.

[3] J. Aller, J. Gallastegui, Analysis of kilometric scale superposed folding in the Central Coal Basin (Cantabrian zone, NW Spain), J. Struct. Geol. 17 (1995) 961–969.

[4] J. Alvarez-Marrón, Three-dimensional geometry and interference of fault-bend folds: Examples from the Ponga Unit, Variscan Belt, NW Spain, J. Struct. Geol. 17 (1995) 549–560.

[5] A.C. Ries, F.R.S. Shackleton, Patterns of strain variation in arcuate fold belts, Phil. Trans. R. Soc. Lond. A283 (1976) 281–287.

[6] S. Marshak, Kinematics of orocline and arc formation in thin-skinned orogens, Tectonics 7 (1988) 73–86.

[7] D.A. Ferrill, R.H. Groshong, Deformation conditions in the northern Subalpine Chain, France, estimated from deformation modes in coarse-grained limestone, J. Struct. Geol. 15 (1993) 995–1006.

[8] D.A. Ferrill, R.H. Groshong, Kinematic model for the curvatrue of the northern subalpine chain, France, J. Struct. Geol. 15 (1993) 523–541.

[9] R. Van der Voo, J.A. Stamatakos, J.M. Parés, Kinematic constraints on thrust–belt curvature from syndeformational magnetizations in the Lagos del Valle Syncline in the Cantabrian Arc, Spain, J. Geophys. Res. 102 (1997) 10105–10119.

[10] D. Hindle, M. Burkhard, Strain, displacement and rotation associated with the formation of curvature in fold belts; the example of the Jura arc, J. Struct. Geol. 21 (1999) 1089–1101.

[11] J. Macedo, S. Marshak, Controls on the geometry of fold–thrust belt salients, Geol. Soc. Am. Bull. 111 (1999) 1808–1822.

[12] A. Pérez-Estaún, F. Bastida, J.L. Alonso, J. Marquínez, J. Aller, J. Alvarez-Marrón, A. Marcos, J.A. Pulgar, A thin-skinned tectonics model for an arcuate fold and thrust belt the Cantabrian Zone (Variscan Ibero–Armorican Arc), Tectonics 7 (1988) 517–537.

[13] L.U. De Sitter, The Hercynian Cantabrian orogen, Mem. Geopaleontol. Univ. Ferrara 1 (1965) 211–225.

[14] M. Julivert, A. Marcos, Superimposed folding under flexural conditions in the Cantabrian zone (Hercynian Cordillera, northwest Spain), Am. J. Sci. 273 (1973) 353–375.

[15] M. Julivert, M.L. Arboleya, A geometrical and kinematical approach to the nappe structure in an arcuate fold-belt: the Cantabrian nappes (Hercynian chain, NW Spain), J. Struct. Geol. 6 (1984) 499–519.

[16] M. Julivert, M.L. Arboleya, Areal balancing and estimate of areal reduction in a thin-skinned fold-and-thrust belt (Cantabrian zone, NW Spain): constraints on its emplacement mechanism, J. Struct. Geol. 8 (1986) 407–414.

[17] N. Bonhommet, P.R. Cobbold, H. Perroud, A. Richardson, Paleomagnetism and cross-folding in a key area of the Asturian Arc (Spain), J. Geophys. Res. 86 (1981) 1873–1887.

[18] H. Perroud, N. Bonhommet, Paleomagnetism of the Ibero–Armorican arc and the Hercynian orogeny in western Europe, Nature 292 (1981) 445–447.

[19] A.M. Hirt, W. Lowrie, M. Julivert, M.L. Arboleya, Paleomagnetic results in support of a model for the origin of the Asturian Arc, Tectonophysics 213 (1992) 321–339.

[20] J.M. Parés, R. Van der Voo, J.A. Stamatakos, A. Pérez-Estaún, Remagnetization and postfolding oroclinal rotations in the Cantabrian/Asturian Arc, northern Spain, Tectonics 13 (1994) 1461–1471.

[21] S.A. Stewart, Paleomagnetic analysis of fold kinematics and implications for geological models of the Cantabrian/Asturias Arc, north Spain, J. Geophys. Res. 100 (1995) 20079–20094.

[22] S.W. Carey, The orocline concept in geotectonics, Proc. R. Soc. Tasman. 89 (1955) 255–289.

[23] A.B. Weil, R. Van der Voo, B.A. van der Pluijm, J.M. Parés, The formation of an orocline by multiple deformations: A paleomagnetic investigation of the Cantabria–Asturias Arc (Cantabria Zone, northern Spain), J. Struct. Geol. 22 (2000) 735–756.

[24] D. Dietrich, H. Song, Calcite fabrics in a natural shear environment, the Helvetic nappes of western Switzerland, J. Struct. Geol. 6 (1984) 19–23.

[25] D. Dietrich, Calcite fabrics around folds as indicators of deformational history, J. Struct. Geol. 8 (1986) 655–668.

[26] J.P. Craddock, A. Kopania, D.V. Wiltschko, Interaction between the northern Idaho–Wyoming thrust belt and bounding basement blocks, central western Wyoming, Geol. Soc. Am. Mem. 171 (1988) 333–351.

[27] T. Engelder, The nature of deformation within the outer limits of the central Appalachian foreland fold and thrust belt in New York State, Tectonophysics 55 (1979) 289–310.

[28] D.V. Wiltschko, D.A. Medwedeff, H.E. Millson, Distribution and mechanisms of strain within rocks on the northwest ramp of the Pine Mountain block, southern Appalachian foreland: A field test theory, Geol. Soc. Am. Bull. 96 (1985) 426–435.

[29] B. Kilsdonk, D.V. Wiltschko, Deformation mechanisms in the southeastern ramp region of the Pine Mountain block, Tennessee, Geol. Soc. Am. Bull. 100 (1988) 653–664.

[30] J.H. Harris, B.A. van der Pluijm, Relative timing of calcite twinning strain and fold–thrust belt development; Hudson Valley fold–thrust belt, New York, USA, J. Struct. Geol. 20 (1998) 21–31.

[31] W.R. Jamison, J.H. Spang, Use of calcite twin lamellae to infer differential stress, Geol. Soc. Am. Bull. 87 (1976) 868–872.

[32] H.R. Wenk, T. Takeshita, E. Bechler, B.G. Erskine, S.

Matthies, Pure shear and simple shear calcite textures. Comparison of experimental, theoretical and natural data, J. Struct. Geol. 9 (1987) 731–745.
[33] F.A. Donath, L.S. Fruth, Dependence of strain rate effects on deformation mechanisms and rock type, J. Geol. 79 (1971) 347–371.
[34] L.W. Teufel, Stain analysis of experimental superposed deformation using calcite twin lamellae, Tectonophysics 65 (1980) 291–309.
[35] A.A. Chinn, R.H. Konig, Stress inferred from calcite twin lamellae in relation to regional structure of northwest Arkansas, Geol. Soc. Am. Bull. 84 (1973) 3731–3736.
[36] J.G. Ramsey, The deformation of early linear structures in areas of repeated folding, J. Geol. 68 (1960) 75–93.
[37] T.J.A. Reijers, Devonian basin-fill histories of the Spanish Cantabrian Mountains and the Belgian Ardennes; a comparison, Geol. Mijnb. 64 (1985) 41–62.
[38] J.G.M. Raven, B.A. van der Pluijm, Metamorphic fluids and transtension in the Cantabrian Mountains of northern Spain; an application of the conodont colour alteration index, Geol. Mag. 123 (1986) 673–681.
[39] F. Bastida, C. Brime, S. Garcia-Lopez, G.N. Sarmiento, Tectono-thermal evolution in a region with thin-skinned tectonics: the western nappes in the Cantabrian Zone (Variscan belt of NW Spain), Int. J. Earth Sci. 88 (1999) 38–48.
[40] D.A. Ferrill, Calcite twin widths and intensities as metamorphic indicators in natural low-temperature deformation of limestone, J. Struct. Geol. 13 (1991) 667–675.
[41] M. Burkhard, Calcite twins, their geometry, appearance and significance as stress–strain markers and indicators of tectonic regime: a review, J. Struct. Geol. 15 (1993) 351–368.
[42] D.A. Ferrill, Critical re-evaluation of differential stress estimates from calcite twins in coarse-grained limestone, Tectonophysics 285 (1998) 77–86.
[43] M. Friedman, D.W. Stearns, Relations between stresses inferred from calcite twin lamellae and macrofractures, Teton Anticline, Montana, Geol. Soc. Am. Bull. 82 (1971) 3151–3162.
[44] G.L. Twombly, J.H. Spang, Experimental test of the calcite strain gage technique at low confining pressure, Tectonophysics 89 (1982) T17–T26.
[45] R.H. Groshong, Experimental test of least square strain gage calculation using twinned calcite, Geol. Soc. Am. Bull. 85 (1974) 1855–1864.
[46] M. Friedman, G.M. Sowers, Petrofabrics: A critical review, Can. J. Earth Sci. 7 (1970) 477–497.
[47] F.J. Turner, Nature and dynamic interpretation of deformation lamellae in calcite of three marbles, Am. J. Sci. 251 (1953) 276–298.
[48] R.H. Groshong, L.W. Teufel, C. Gasteiger, Precision and accuracy of the calcite strain–gauge technique, Geol. Soc. Am. Bull. 95 (1984) 357–363.
[49] R.H. Groshong, Strain calculated from twinning in calcite, Geol. Soc. Am. Bull. 83 (1972) 2025–2038.
[50] M.A. Evans, R.H. Groshong, A computer program for the calcite-strain technique, J. Struct. Geol. 16 (1994) 277–282.
[51] S.Y. Schwartz, R. Van der Voo, Paleomagnetic evaluation of the orocline hypothesis in the central and southern Appalachians, Geophys. Res. Lett. 10 (1983) 505–508.
[52] P. Matte, Tectonics and plate tectonics model for the Variscan belt of Europe, Tectonophysics 126 (1986) 329–374.
[53] M. Julivert, J. Truyols, J. García-Alcalde, Mapa Geológico de España E 1:200 000 2nd Serie, Hoja No 10, Meires, Instituto Geologico y Minero de España, Madrid, 1981.